Probing the bulk plasmon continuum of layered materials through electron energy loss spectroscopy in a reflection geometry

Christian Boyd, Luke Yeo, and Philip W. Phillips[*]

Department of Physics and Institute for Condensed Matter Theory, University of Illinois 1110 W. Green Street, Urbana, Illinois 61801, USA

A periodic arrangement of two-dimensional (2D) conducting planes is known to host a (bulk) plasmon dispersion that interpolates between the typical, gapped behavior of three-dimensional (3D) metals and a gapless, acoustic regime as a function of the out-of-plane wave vector. The semi-infinite system—the configuration relevant to electron energy loss spectroscopy (EELS) in a reflection geometry, as in high-resolution EELS (HREELS)—is known to host a surface plasmon that ceases to propagate below a cutoff wave vector. As the f-sum rule requires a finite response whether there exist sharp excitations, we demonstrate that what remains in the surface loss function—the material response probed by HREELS—is the contribution from the (bulk) plasmon of the infinite system. We provide a one-to-one mapping between the plasmon continuum and the spectral weight in the surface loss function. In light of this result, we suggest that HREELS be considered a long-wavelength probe of the plasmon continuum in layered materials.

I. INTRODUCTION

In the mid-1970s, Fetter [1] applied a hydrodynamic analysis to a periodic system of conducting planes, each hosting a two-dimensional (2D) electron gas, and obtained a rather unique plasmon continuum. The *plasmon*—the long-wavelength oscillation of the many-electron charge density—radically changes in character depending on whether adjacent conducting planes of the system are oscillating in-phase or out-of-phase. While the in-phase oscillation [see Fig. 1(a)] corresponds to a gapped (optical) mode reminiscent of plasmons in simple three-dimensional (3D) metals, the out-of-phase oscillation [see Fig. 1(b)] corresponds to a gapless (acoustic) mode that disperses linearly with an in-plane wave vector. Between the extremes of in-phase and out-of-phase oscillation lies an acoustic-to-optical plasmon continuum (see Fig. 2).

Due to the severe conduction anisotropy in the high-T_C cuprate superconductors [2–5], doped cuprates are often modeled as a system of copper oxide planes, i.e., the model studied by Fetter. Significant experimental effort has recently been invested toward demonstrating that doped cuprates exemplify the plasmon continuum scenario using resonant inelastic x-ray scattering (RIXS) on both electron-doped cuprates, such as $La_{2-x}Ce_xCuO_4$ and $Nd_{2-x}Ce_xCuO_4$ [6,7], as well as the hole-doped compounds $La_{2-x}Sr_xCuO_4$ (LSCO) and $Bi_2Sr_{1.6}La_{0.4}CuO_{6+\delta}$ (Bi-2201) [8,9]. Shared among these RIXS studies is a peak in the scattered intensity whose (planar) wave vector dispersion changes appreciably as the out-of-plane wave vector is tuned toward an out-of-phase oscillation between adjacent copper oxide layers. By identifying this peak with the plasmon, RIXS data provide strong evidence of a nearly acoustic mode in doped cuprates coincident with the out-of-phase, acoustic plasmon dispersion of the Fetter model. This analogy to the Fetter model can be completed by tracking the evolution toward the optical plasmon dispersion when the out-of-plane wave vector corresponds to in-phase oscillation; however, the scattering geometry and suppression of charge excitations at a large out-of-plane wave vector in the RIXS cross-section make this connection difficult to establish concretely [10].

Rather than following the (3D) wave vector dispersion of charge density excitations, we instead consider an experimental probe that lacks translation symmetry along a chosen axis: electron energy loss spectroscopy (EELS) in a *reflection* geometry; i.e., high-resolution EELS (HREELS). When the reflection surface is perpendicular to the out-of-plane (layering) direction, the explicitly broken translation symmetry renders HREELS, in principle, susceptible to all out-of-plane wave vector contributions, a point previously made in Refs. [11,12]. Our main result is that EELS in a reflection geometry (HREELS) does, in fact, probe the bulk plasmon continuum of the Fetter model in the long-wavelength limit. As a consequence, layered materials should generically be expected to host a broad surface response at long wavelengths due to their underlying bulk plasmon continuum.

While the doped cuprates provide motivation for this investigation, these compounds are notoriously complex. Because of its relative simplicity and close correspondence to the plasmon behavior seen in RIXS, we will instead focus on the Fetter model of layered conducting planes (e.g., as was also done in Ref. [13]). Though the aforementioned studies [6–9] contain more involved computational analyses to fit their experimental curves, the qualitative plasmon behavior (or treatment of the Coulomb interaction) often mirrors the Fetter result [1]. One could argue that the Fetter model might represent a pathological limit since it neglects interplane
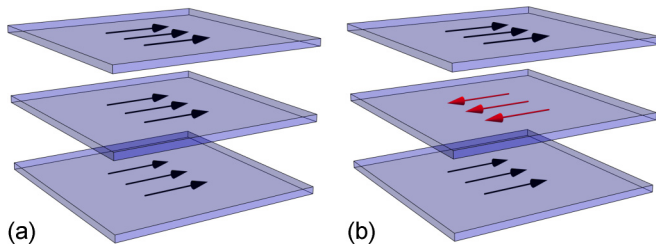
*dimer@illinois.edu

FIG. 1. A visual representation of the (a) in-phase and (b) out-of-phase charge oscillation within a periodic system of conducting planes.

conduction; however, the inclusion of interlayer electron hopping results in a plasmon dispersion that continuously evolves from the Fetter result into a more general anisotropic dispersion [14]. This is to say that our results apply inasmuch as the Fetter model is capable of describing any particular (strongly) anisotropic system.

II. THE SEMI-INFINITE FETTER MODEL

In our implementation of the Fetter model, we consider a system of conducting planes separated by (insulating) dielectric layers, i.e., a semi-infinite, single-layer superlattice (see Fig. 3). The conducting planes are characterized by a long wavelength, 2D Drude conductivity σ at frequency ω through the standard relation:

$$\sigma(\omega) = \frac{ine^2}{m\omega\left(1 + \frac{i}{\omega\tau}\right)},\tag{1}$$

where n is the 2D (planar) electron density, e the electron charge, m the electron mass, and τ corresponds to a relaxation time associated with electron scattering. The layer periodicity of the 2D conducting planes (or the interlayer distance) is denoted by a, and we model the insulating, dielectric regions through a dielectric constant $\epsilon > 1$.

The excitations of the infinite Fetter model—the periodic system of conducting planes without boundary—are well studied. In the limit of negligible conduction dissipation ($\omega_p\tau \gg 1$), the bulk plasmon dispersion with the in-plane wave vector q and out-of-plane wave vector Q is given by [1,15–19]

$$\omega_p(q, Q) = \Omega\sqrt{\frac{qa \sinh qa}{2\cosh qa - 2\cos Qa}},\tag{2}$$

where Ω is the optical plasma frequency defined as

$$\Omega^2 := \frac{ne^2}{\epsilon_0\epsilon ma}.\tag{3}$$

The ω_p dispersion in Eq. (2) is plotted in Fig. 2.

In the semi-infinite geometry (i.e., as in Fig. 3), bulk plasmons are no longer self-sustained resonances of the system due to the lack of translation symmetry in the out-of-plane direction. Instead, *surface plasmons*—planar charge density oscillations that decay away from the vacuum-material interface—are the long-lived excitations of the superlattice. When corrections due to the finite relaxation time τ are negligible, the surface modes follow the dispersion relation
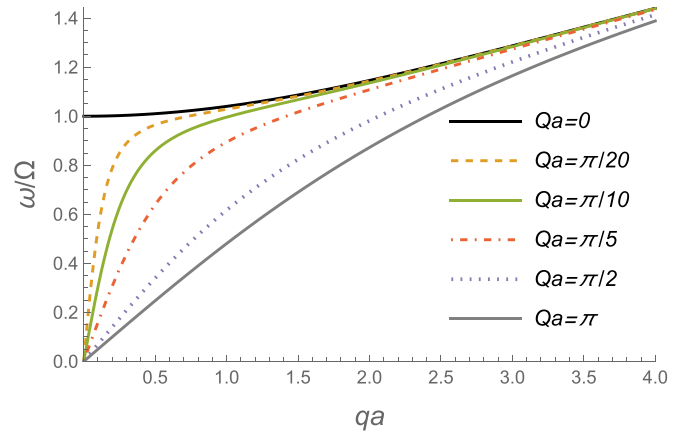

FIG. 2. Plotted above is the dispersion of the plasma frequency ω_p in Eq. (2) for a periodic system of two-dimensional (2D) conducting planes. The frequency scale is in units of optical plasma frequency Ω in Eq. (3). The in-plane wave vector q and out-of-plane wave vector Q are given in units of interplane separation a.

[16,17,19]:

$$\omega_{sp}(q) = \Omega\sqrt{\frac{qa\epsilon[\epsilon\cosh qa - \sinh qa]}{(\epsilon^2 - 1)\sinh qa}},\tag{4}$$

whose functional form depends on the dielectric mismatch at the vacuum-material interface. The ω_{sp} dispersion in Eq. (4) is plotted in Fig. 4. Curiously, the surface plasmon ceases to exist for sufficiently long wavelengths and is never a resonance of the system in the absence of a dielectric background [20]. The cutoff wave vector q^*:

$$q^*a := \ln\left(\frac{\epsilon + 1}{\epsilon - 1}\right),\tag{5}$$

marks the lower bound for surface plasmon propagation at a given $\epsilon > 1$ [15,17,19].

III. DIELECTRIC ANALYSIS

The lack of long-lived charge density excitations in the $q < q^*$ regime of the semi-infinite Fetter model poses an
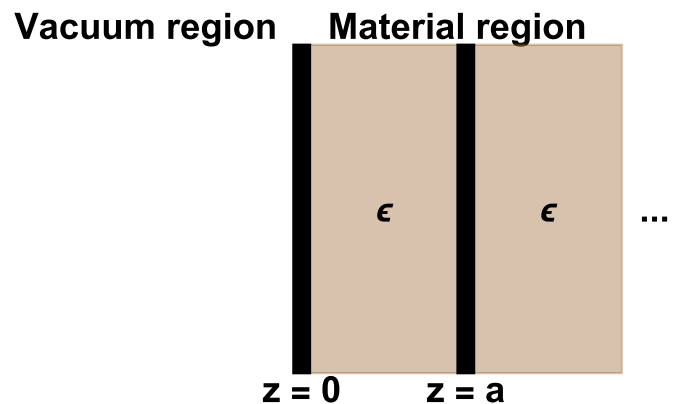

FIG. 3. The semi-infinite model of periodic conducting planes—the semi-infinite Fetter model—considered in this paper. The thick black lines denote two-dimensional (2D) conducting planes, the dielectric constant within the insulating layers is denoted by ϵ, and the layer periodicity is given by a.
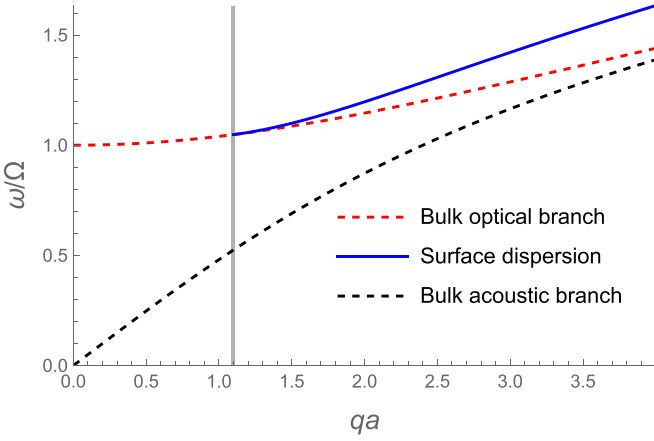
FIG. 4. Dispersion of the surface plasma frequency ω_{sp} in Eq. (4) in the semi-infinite Fetter model (solid line) for the value $\epsilon = 2$. The bulk optical and acoustic branches (dashed lines) are obtained from the plasma frequency $\omega_p(q, Q)$ in Eq. (2) at $Qa = 0$ and π, respectively. The vertical bar denotes the cutoff wave vector q^*a, determined by ϵ through Eq. (5), below which the surface plasmon ceases to propagate.

interesting question for a HREELS experiment: What does HREELS measure at wave vectors below q^*? Independent of sharp excitations, the spectral weight in the (dissipative) density response for $q < q^*$ is nevertheless constrained by the f-sum rule in a reflection geometry [21–26]. Put simply, HREELS has to measure something associated with charge density excitations at long wavelengths—and a fixed amount of it. It has previously been found that, in addition to the surface plasmon, there is a finite contribution from the bulk plasmon [27,28]; however, the bulk correction typically constitutes a weak or visually imperceptible shoulder in the surface loss function above the (bulk) plasma frequency. To quantify the redistribution of spectral weight in the $q < q^*$ regime of the semi-infinite Fetter model, we study the surface loss function:

$$g(q, \omega) := -\frac{e^2}{2\epsilon_0|q|} \int_0^\infty dz dz'$$
$$\times \chi''(q, \omega; z, z') \exp(-|q|z) \exp(-|q|z'), \quad (6)$$

since this dimensionless quantity captures the material response contribution to the HREELS cross-section [25,29–31]. In Eq. (6), χ'' denotes the imaginary part of the density response function χ which has been Fourier transformed along the planar and temporal directions, i.e., we assume planar translation invariance, and the material region is chosen as the half-space $z > 0$.

As our implementation of the semi-infinite Fetter model (see Fig. 3) is made up of alternating conducting and dielectric layers, we calculate the surface loss function in Eq. (6) through a dielectric analysis of the system. In the dielectric theory of reflection EELS [30,32–34] (and the vacuum scattering contributions in Refs. [29,35]), one characterizes the system through local dielectric response (in the out-of-plane, or layering, direction) and derives the long-ranged effect of the Coulomb interaction by enforcing electromagnetic boundary conditions across each interface. Superlattice

boundary conditions are often written in the full electrodynamic formalism in terms of the electric and magnetic field vectors [15,16,36]. Instead, we take the nonretarded limit $q^2 \gg \omega^2/c^2$ from the outset and work in a theory of potentials ϕ, ϕ_D for the electric field $E = -\nabla\phi$ and the electric displacement $D = -\epsilon_0\nabla\phi_D$, which are themselves related in the dielectric regions through $D = \epsilon_0\epsilon E$. At each interface, we have the standard boundary conditions that the planar components of E are continuous and, across a conducting plane, that the discontinuity in the D_z is given by the planar charge density. By use of the continuity equation and recognizing that the finite (q, ω) components of the planar charge density are entirely due to the induced response, the discontinuity in D_z can be related to the planar components of E and the conductivity σ. Lastly, the infinite system of boundary conditions can be closed by requiring decaying (bounded) behavior for ϕ, ϕ_D within the material (e.g., see Refs. [16,19]).

The dielectric analysis provides calculational utility since the surface loss function in Eq. (6) is encoded in the vacuum solution for the electric potential when a driving field is applied [25,33,37,38]. To be concrete, consider a semi-infinite system whose boundary is defined by a barrier to its charge density at $z = 0$, as in our Fetter model of Fig. 3, and is embedded within a dielectric medium characterized by ϵ. If a perturbing potential ϕ_{ext} is sourced by a charge density localized entirely within the vacuum region (implementing the negligible material penetration assumption used to construct the HREELS cross-section [30–32]), then the material responds to a field of the form:

$$\phi_{ext}(q, \omega, z > 0) = C_{ext}(q, \omega) \exp(-|q|z), \quad (7)$$

by inducing the charge density:

$$\rho_{ind}(q, \omega, z) = e^2 C_{ext}(q, \omega) \int_{z'>0} dz'$$
$$\times \chi(q, \omega; z, z') \exp(-|q|z'), \quad (8)$$

via the definition of the density response function χ. Outside of the material (in the vacuum region $z < 0$), the induced charge density in Eq. (8) sources an induced potential:

$$\phi_{ind}(q, \omega, z < 0) = \frac{e^2}{2\epsilon_0|q|} \left(\frac{2}{1+\epsilon}\right) C_{ext}(q, \omega) \exp(+|q|z)$$
$$\times \int_0^\infty dz' dz'' \chi(q, \omega; z', z'')$$
$$\times \exp(-|q|z') \exp(-|q|z''). \quad (9)$$

In Eq. (9), ϕ_{ind} depends on ϵ through the boundary conditions across $z = 0$. Already, the induced potential in vacuum in Eq. (9) is probing the density response function in the same way as the surface loss function in Eq. (6).

To extract the surface loss function from the induced potential in Eq. (9), we require an explicit form of the external field coefficient C_{ext} in Eq. (7). A convenient external field—ϕ_{ext} of Eq. (7)—to consider is the classical dielectric description of EELS in a reflection geometry [33,39,40], wherein an incoming electron is modeled by a trajectory that undergoes elastic reflection off the material surface ($z = 0$) at the time $t = 0$. The potential ϕ_{ext} sourced by this classical electron

trajectory is

$$\phi_{\text{ext}}(q, \omega, z < 0) = A(q, \omega) \cos\left[(\omega - q \cdot v_\parallel)\left(\frac{z}{v_z}\right)\right]$$
$$- \left(\frac{\epsilon}{1 + \epsilon}\right) A(q, \omega) \exp(+|q|z) \quad (10)$$

in the vacuum region and

$$\phi_{\text{ext}}(q, \omega, z > 0) = \left(\frac{1}{1 + \epsilon}\right) A(q, \omega) \exp(-|q|z) \quad (11)$$

in the material region. In Eqs. (10) and (11), dependence on ϵ is through the boundary conditions across $z = 0$, the coefficient A is defined by

$$A(q, \omega) := -\frac{2ev_z}{\epsilon_0[q^2 v_z^2 + (\omega - q \cdot v_\parallel)^2]}, \quad (12)$$

and the reflection trajectory of the classical electron is parameterized by its velocity components $v_\parallel$ and v_z, which are, respectively, parallel and perpendicular to the ($z = 0$) surface. In light of Eq. (11), we can immediately write down the material response (in vacuum) to this particular ϕ_{ext} using Eq. (9) through the replacement $C_{\text{ext}} \to A/(1 + \epsilon)$ as

$$\phi_{\text{ind}}(q, \omega, z < 0) = \frac{e^2}{2\epsilon_0|q|} \frac{2}{(1 + \epsilon)^2} A(q, \omega) \exp(+|q|z)$$
$$\times \int_0^\infty dz' dz'' \chi(q, \omega; z', z'')$$
$$\times \exp(-|q|z') \exp(-|q|z''). \quad (13)$$

The vacuum response of the material in Eq. (13) provides a recipe to calculate the surface loss function within a dielectric model. Since A in Eq. (12) is real [and as a result, so is ϕ_{ext} in Eq. (10) in vacuum], the imaginary part of the total potential $\phi_{\text{tot}} := \phi_{\text{ind}} + \phi_{\text{ext}}$ is solely through the material contribution in ϕ_{ind}. From the definition of the surface loss function in Eq. (6), only the imaginary contribution of the material response is needed, and we can extract this quantity from the total vacuum potential ϕ as

$$g(q, \omega) = -\left[\frac{(1 + \epsilon)^2}{2A(q, \omega)}\right] \text{Im} \, \phi(q, \omega, z = 0)$$
$$= -\left[\frac{(1 + \epsilon)^2}{2A(q, \omega)}\right] \text{Im} \, \phi_{\text{ind}}(q, \omega, z = 0), \quad (14)$$

even when the $\phi_{\text{ind}}, \phi_{\text{ext}}$ are not known separately. Naturally, the (total) potential ϕ associated with the electric field can be obtained through a dielectric analysis of the semi-infinite Fetter model, and the calculation of the surface loss function reduces to using Eq. (14) on the vacuum solution.

IV. RESULTS

Upon applying the aforementioned electromagnetic boundary conditions to our implementation of the semi-infinite Fetter model, we can extract the surface loss function g from the vacuum potential ϕ through the relation given in Eq. (14). The surface loss function can be separated into two components:

$$g(q, \omega) = g_s(q, \omega) + g_b(q, \omega), \quad (15)$$

where

$$g_s(q, \omega) := \frac{(1 + \epsilon)^2}{4} \text{Im} \, \frac{2\bar{q}\epsilon^2 s \cosh \bar{q} - (2\bar{\omega}^2 \epsilon^2 + \bar{q}\epsilon s) \sinh \bar{q}}{\bar{q}\epsilon^2 s \cosh \bar{q} - [(\epsilon^2 - 1)\bar{\omega}^2 + \bar{q}\epsilon s] \sinh \bar{q}} \quad (16)$$

and

$$g_b(q, \omega) := \frac{(1 + \epsilon)^2}{4} \text{Im} \, \frac{\epsilon \sqrt{\sinh \bar{q}[(4\bar{\omega}^4 + \bar{q}^2 s^2) \sinh \bar{q} - 4\bar{q}\bar{\omega}^2 s \cosh \bar{q}]}}{\bar{q}\epsilon^2 s \cosh \bar{q} - [(\epsilon^2 - 1)\bar{\omega}^2 + \bar{q}\epsilon s] \sinh \bar{q}} \quad (17)$$

are loosely associated with surface (g_s) and bulk (g_b) plasmon excitation; similar decompositions have been previously noted [17,27,28]. In the definitions of g_s in Eq. (16) and g_b in Eq. (17), the dimensionless parameters $\bar{q} := qa, \bar{\omega} := \omega/\Omega, s := (1 + i/\omega\tau)^{-1}$ have been introduced, Ω is the optical plasma frequency in Eq. (3), and the assumption $\epsilon > 1$ has been used. Additionally, the complex square root in the definition of g_b in Eq. (17) corresponds to the branch with a positive imaginary part.

At sufficiently large $q > q^*$, the essential behavior of the surface g_s in Eq. (16) and bulk g_b in Eq. (17) contributions to the surface loss function g can be gleaned from their identical pole structure. Notably, both g_s and g_b have the same denominator that, in the $s \to 1$ ($\tau \to \infty$) limit, can be written as

$$\frac{1}{\bar{q}\epsilon^2 \cosh \bar{q} - [(\epsilon^2 - 1)\bar{\omega}^2 + \bar{q}\epsilon] \sinh \bar{q}}$$
$$= \left[\frac{1}{(\epsilon^2 - 1) \sinh \bar{q}}\right] \frac{1}{\frac{\omega_{sp}^2(q)}{\Omega^2} - \bar{\omega}^2} \quad (18)$$

in terms of the surface plasma frequency ω_{sp} of Eq. (4). If the relaxation time τ is not short enough to radically alter the surface plasmon dispersion, both the surface g_s and bulk g_b terms peak at $\omega = \omega_{sp}$. When the surface plasmon is a sharp resonance of the semi-infinite Fetter model (i.e., for q sufficiently larger than q^*), both g_s and g_b appear similar in character and simply provide two contributions to the spectral weight at the surface plasma frequency ω_{sp}. This behavior can be seen at $qa = 4$ in Fig. 5(a); the g_s, g_b curves lie atop one another, and the cutoff wave vector $q^*a = \ln 3 \approx 1.1$ [from Eq. (5) using $\epsilon = 2$ of Fig. 5] is suitably smaller than $qa = 4$.

When $q > q^*$ approaches q^*, the distinction between g_s and g_b becomes apparent as the square root in the numerator of g_b in Eq. (17) begins to appreciably contribute. In the $s \to 1$ ($\tau \to \infty$) limit, the quartic polynomial in $\bar{\omega}$ within the square root of Eq. (17):

$$(4\bar{\omega}^4 + \bar{q}^2) \sinh \bar{q} - 4\bar{q}\bar{\omega}^2 \cosh \bar{q}, \quad (19)$$
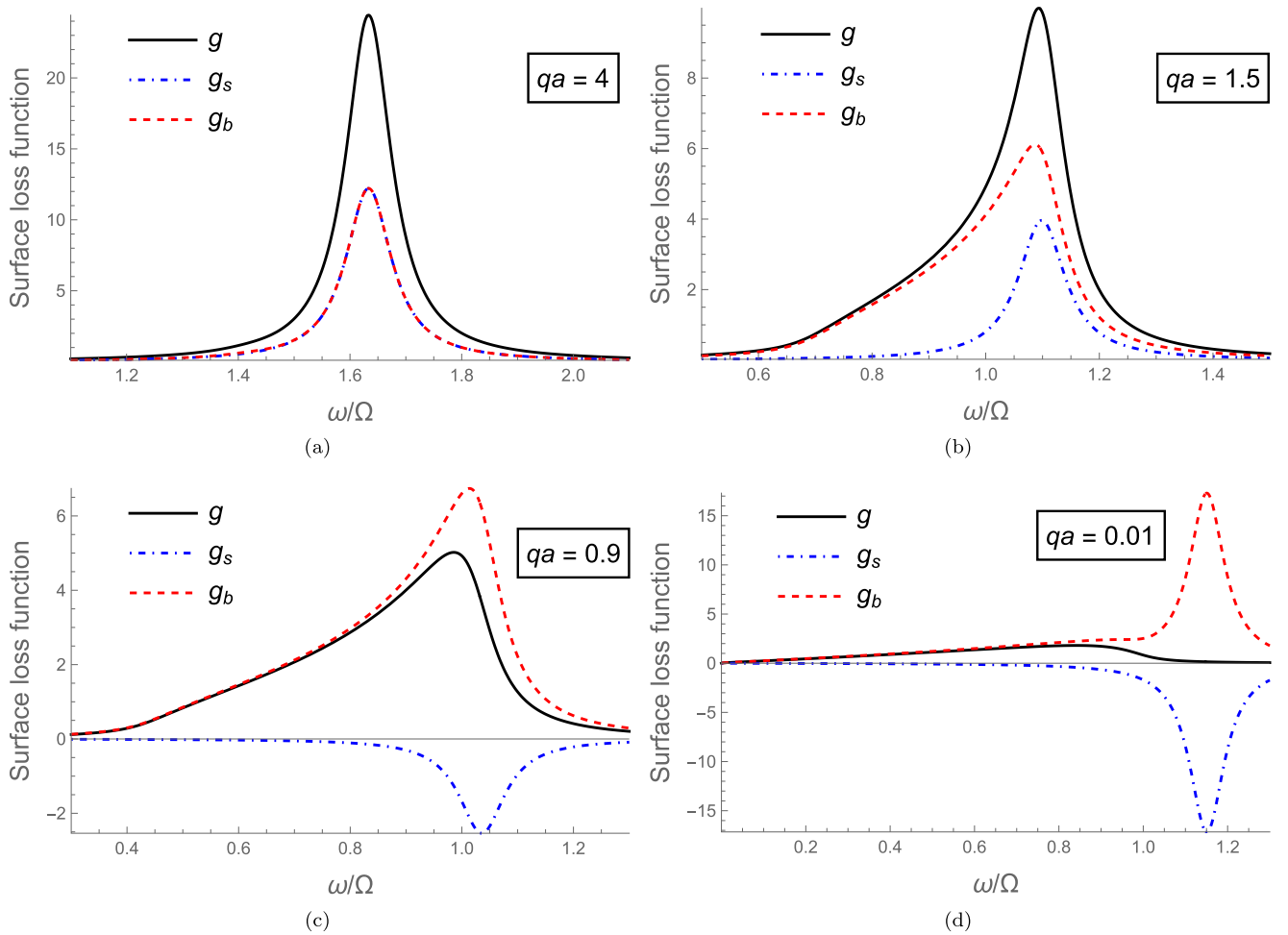
FIG. 5. Surface loss function $g = g_s + g_b$ of Eq. (15), at $\epsilon = 2$ and $\tau = 10/\Omega$ across several values of the in-plane wave vector q. At $\epsilon = 2$, the cutoff wave vector is given by Eq. (5) as $q^*a = \ln 3 \approx 1.1$. At each wave vector, the surface plasma frequency ω_{sp} and continuum of bulk plasma frequencies can be determined by Eqs. (4) and (2), respectively. In (a), $qa = 4$ ($q > q^*$), $\omega_{sp} \approx 1.63\,\Omega$, and the plasmon continuum spans $1.39\,\Omega < \omega < 1.44\,\Omega$. In (b), $qa = 1.5$ ($q > q^*$), $\omega_{sp} \approx 1.10\,\Omega$, and the plasmon continuum spans $0.69\,\Omega < \omega < 1.09\,\Omega$. In (c), $qa = 0.9$ ($q < q^*$), $\omega_{sp} \approx 1.04\,\Omega$ is nonpropagating, and the plasmon continuum spans $0.44\,\Omega < \omega < 1.03\,\Omega$. In (d), $qa = 0.01$ ($q < q^*$) is the $qa \to 0$ limit, $\omega_{sp} \approx 1.15\,\Omega$ is nonpropagating, and the plasmon continuum spans $0 < \omega < \Omega$.

has the zeros

$$\omega = \omega_p(q, Q = 0) \quad \text{and} \quad \omega = \omega_p(q, Q = \pi/a). \quad (20)$$

In Eq. (20), ω_p is the bulk plasma frequency given by Eq. (2), and Q labels the out-of-plane wave vector of the bulk plasmon in the infinite Fetter model. Even in the $s \to 1$ limit, the square root in the definition of g_b in Eq. (17) contributes a finite imaginary part when ω is within the bulk plasmon continuum, or $\omega_p(q, Q = \pi/a) < \omega < \omega_p(q, Q = 0)$. The bulk part ($g_b$) of the surface loss function g then is made up of two contributions: a peak at the surface plasma frequency $\omega = \omega_{sp}$ and a continuum of modes across the bulk plasmon dispersion $\omega_p(q, Q)$ in Eq. (2) at fixed in-plane q. The contribution of both bulk and surface modes can be observed in Fig. 5(b) at $qa = 1.5$, where the chosen value of $\epsilon = 2$ still maintains $qa > q^*a = \ln 3 \approx 1.1$ from Eq. (5).

For $q < q^*$, the surface plasmon is no longer a self-sustained resonance of the semi-infinite Fetter model: this is how q^* in Eq. (5) is defined. The lack of surface plasmon propagation is a precise statement occurring at q^* if finite-τ

corrections to the surface plasmon dispersion are negligible [17,19,41]; however, the spectrum itself evolves continuously across $q = q^*$ [42]. Nevertheless, there is a sharp, qualitative change in the surface contribution g_s across $q = q^*$. From the definition of g_s in Eq. (16) at finite τ (i.e., not in the $s \to 1$ limit), g_s is proportional to the frequency-independent factor:

$$g_s(q, \omega) \propto [-2\epsilon \cosh qa + (1 + \epsilon^2) \sinh qa], \quad (21)$$

which vanishes at the cutoff wave vector $q = q^*$ of Eq. (5). For $q > q^*$, the multiplicative factor in Eq. (21) is positive, whereas it is negative for $q < q^*$. Naturally, the total surface loss function $g = g_s + g_b$ cannot become negative, as the density response in Eq. (6) is related to a sum of transition amplitudes for charge density excitations via the fluctuation-dissipation theorem. Instead, the sign change across $q = q^*$ represents a kind of inverse begrenzungs effect [34,43], wherein the surface component g_s suppresses spectral weight at the (nonpropagating) surface plasma frequency arising from the pole in g_b at $\omega = \omega_{sp}$. The net effect of the suppression at $\omega = \omega_{sp}$ is to increase the relative contribution
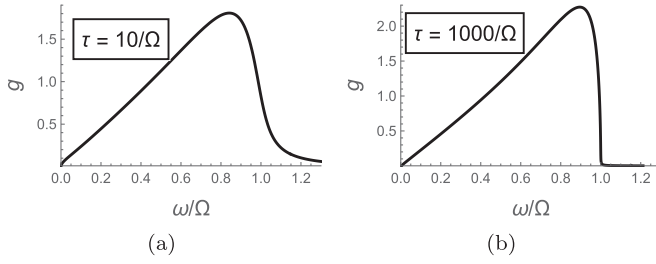
FIG. 6. Surface loss function $g = g_s + g_b$ at $\epsilon = 2$ and the $qa \to 0$ limit implemented by $qa = 0.01$. In (a), g from Fig. 5(d) ($\tau = 10/\Omega$) is plotted on its own for clarity. In (b), g is plotted for the same $\epsilon = 2$ and $qa = 0.01$ but at the much longer relaxation time $\tau = 1000/\Omega$. In the $qa \to 0$ limit, the bulk plasmon continuum is bounded by $0 < \omega < \Omega$ from Eq. (2).

from the bulk plasmon continuum to the (total) surface loss function g. This behavior can be observed in Fig. 5(c) at $qa = 0.9 < q^*a = \ln 3 \approx 1.1$ for the chosen value $\epsilon = 2$.

In the $qa \to 0$ limit, the nonpropagating surface plasmon peak at $\omega = \omega_{sp}$ becomes increasingly suppressed, leaving only a broad response across the bulk plasmon continuum $0 < \omega < \Omega$. This behavior can be observed in Fig. 5(d) for $qa = 0.01$ and $\epsilon = 2$: there is no appreciable feature in the surface loss function g at the peak $\omega = \omega_{sp}$ visible for either g_s or g_b. As the vertical scale due to g_b and g_s obscures g in Fig. 5(d), g is plotted by itself in Fig. 6(a). Curiously, the broad response across the bulk plasmon continuum is relatively insensitive to the relaxation time τ if the plasmon dispersion is not noticeably altered from its free electron value in Eq. (2). In Fig. 6(b), the surface loss function g is plotted for the same $qa \to 0$ limit ($qa = 0.01$) and dielectric constant $\epsilon = 2$ but at the long relaxation time $\tau = 1000/\Omega$; notwithstanding, the broad shape across $0 < \omega < \Omega$ remains, and the only qualitative difference is the loss of curvature near $\omega = 0, \Omega$ when compared with g at $\tau = 10/\Omega$ in Fig. 6(a). The low energy, linear tail and broad peak near but not at the optical plasma frequency Ω appear as signatures of the underlying bulk plasmon continuum rather than resulting from any particular damping factor. While this statement is qualitatively general, it should be noted that the precise shape of the surface loss function in the $qa \to 0$ limit is sensitive to the dielectric constant ϵ. In Fig. 7, the $qa \to 0$ surface loss function is shown at $\epsilon = 1.1, 2, 5,$ and 10 to demonstrate the influence of ϵ on the spectrum.

In addition to the surface loss function having support across the (bulk) plasmon continuum, the induced potential at these energies oscillates in step with the associated plasmon. Through our dielectric analysis, we can provide a precise, one-to-one correspondence between the plasmon at out-of-plane wave vector Q—$\omega_p(q, Q)$ of Eq. (2)—and the material response at fixed q across the plasmon continuum. In the dielectric theory, this out-of-plane oscillation occurs in the decay factor $\exp[-\beta a]$, which relates the potential in adjacent dielectric layers: $\phi_n = \exp[-\beta a]\phi_{n+1}$. To maintain a bounded solution as $n \to \infty$, we require $\mathrm{Re}\,\beta \geqslant 0 \iff |\exp[-\beta a]| \leqslant 1$; decaying modes (surface plasmons) correspond to $|\exp[-\beta a]| < 1$, whereas wavelike modes (bulk plasmons) correspond to $|\exp[-\beta a]| = 1$ [16,19,44]. In the $\tau \to \infty$ limit of negligible conductivity dissipation, the decay
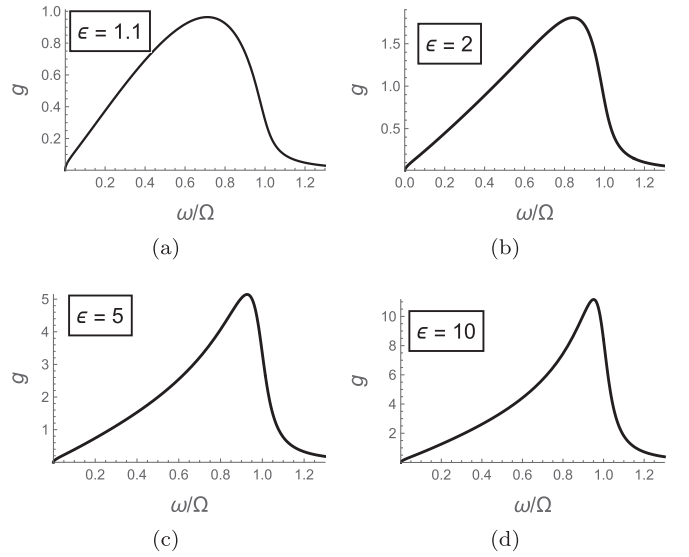

FIG. 7. Variation of the $qa \to 0$ ($qa = 0.01$) surface loss function g in Eq. (15) with the dielectric constant ϵ. The parameters used are $\tau = 10/\Omega$ and: (a) $\epsilon = 1.1$ ($q^*a \approx 3.0$), (b) $\epsilon = 2$ ($q^*a \approx 1.1$), (c) $\epsilon = 5$ ($q^*a \approx 0.41$), and (d) $\epsilon = 10$ ($q^*a \approx 0.20$). The value ϵ determines q^* through Eq. (5).

factor across the plasmon continuum is determined solely by the out-of-plane oscillation of the (bulk) plasmon. Specifically, rearranging the plasmon dispersion ω_p in Eq. (2):

$$\cos Qa = \frac{1}{2}\left[2\cosh qa - \left(\frac{\Omega}{\omega}\right)^2 qa \sinh qa \right], \qquad (22)$$

enables us to label the bulk plasmon at fixed (q, ω) through its out-of-plane wave vector Q. Using the prescription in Eq. (22), we find that $\exp[-\beta a] = \exp[-iQa]$ at energies satisfying the plasmon dispersion $\omega_p(q, Q)$ of Eq. (2). In Fig. 8, we demonstrate this behavior by plotting the decay factor $\exp[-\beta a]$ across the bulk plasmon continuum at $qa = 0.5$, $\epsilon = 2$, and in the $\tau \to \infty$ limit. For clarity, the equivalence $\exp[-\beta a] = \exp[-iQa]$ is maintained at arbitrary in-plane wave vector qa and dielectric constant $\epsilon > 1$ across the bulk plasmon continuum. The surface loss function then is a direct probe of the (bulk) plasmon across $\omega_p(q, Q)$ at fixed in-plane q.
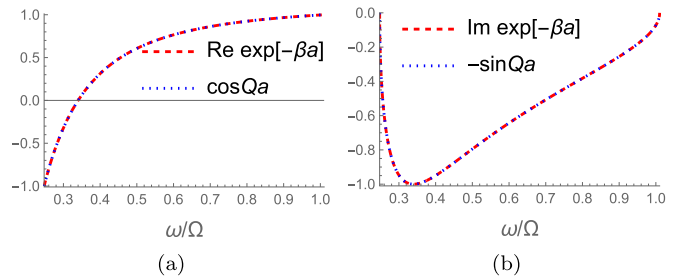

FIG. 8. (a) Real and (b) imaginary parts of the decay factor $\exp(-\beta a)$ to demonstrate the equality between the out-of-plane oscillation in the electric potential and the out-of-plane wave vector Q in Eq. (22) across the plasmon continuum. The parameters used are $qa = 0.5$, $\epsilon = 2$, and the $\tau \to \infty$ limit. In both (a) and (b), the two curves lie atop one another.

The surface loss function g in Eq. (15) demonstrates the transition from surface plasmon propagation at large in-plane wave vectors to a long-wavelength regime dominated by the bulk plasmon continuum (see Fig. 5). Instead of a sharp peak at a single frequency, the $qa \to 0$ surface loss function is characterized by a linear tail at low energies and a broad peak across the (bulk) plasmon continuum. This shape is only weakly influenced by the intrinsic damping parameter (see Fig. 6); however, the spectrum is sensitive to the dielectric constant ϵ (see Fig. 7). Though the bulbous peak might initially suggest a damped, residual surface plasmon at long wavelengths, the oscillatory behavior of the electric potential across the plasmon continuum (e.g., the exact correspondence $\exp[-\beta a] = \exp[-iQa]$ demonstrated in Fig. 8) suggests that the broad spectrum is intrinsic to the plasmon itself. From this perspective, we find that the long-wavelength surface loss function is purely a bulk probe of the semi-infinite Fetter model.

V. DISCUSSION

Authors of previous studies [17,27,28,33,40,42,45–48] have demonstrated and emphasized that bulk charge density excitations appear in the surface loss function (i.e., the HREELS cross-section); however, the contribution of bulk excitations typically presents as either a weak, possibly imperceptible, shoulder near sharp surface excitations or a broad background. We found similar behavior in the semi-infinite Fetter model for sufficiently large (in-plane) wave vectors. At $qa = 1.5 > q^*a$ in Fig. 5(b), a shoulder forms across the bulk plasmon continuum before the strong peak at the surface plasma frequency. Just below the cutoff wave vector ($q < q^*$) in Fig. 5(c), however, the peak at the (nonpropagating) surface plasma frequency has become suppressed, and the surface loss function takes on a broad shape across the bulk plasmon continuum. In the long-wavelength limit ($qa \to 0$), the peak at the (nonpropagating) surface plasma frequency is visible in both g_s and g_b in Fig. 5(d), yet no such feature appears in the surface loss function $g = g_s + g_b$ of Fig. 6(a). In essence, the long-wavelength surface loss function of the semi-infinite Fetter model probes only the bulk plasmon continuum of the infinite system.

In the absence of a propagating surface plasmon, the transfer of spectral weight to the bulk plasmon continuum is required by the f-sum rule. While we have performed a dielectric analysis, the electromagnetic response encoded within the vacuum potential in Eq. (14) genuinely behaves as the many-body response function defined in Eq. (6). The f-sum rule:

$$\int_0^\infty d\omega\, \omega\, g(q,\omega) = \frac{\pi e^2 |q|}{4\epsilon_0 m} \int_0^\infty dz\, n(z) \exp(-2|q|z), \quad (23)$$

relates the spectral weight within the surface loss function g in Eq. (6) of our layered model to the electron density $n(z)$. Notably, the f-sum rule in Eq. (23) is reduced when compared with its standard form [21,24,25,28] due to the lack of out-of-plane dispersion in the semi-infinite Fetter model (e.g., see the derivation in Ref. [49]). As a system of regularly spaced conducting planes, the electron density in our analysis is simply $n(z) = n \sum_j \delta(z - ja)$, where n is the planar electron
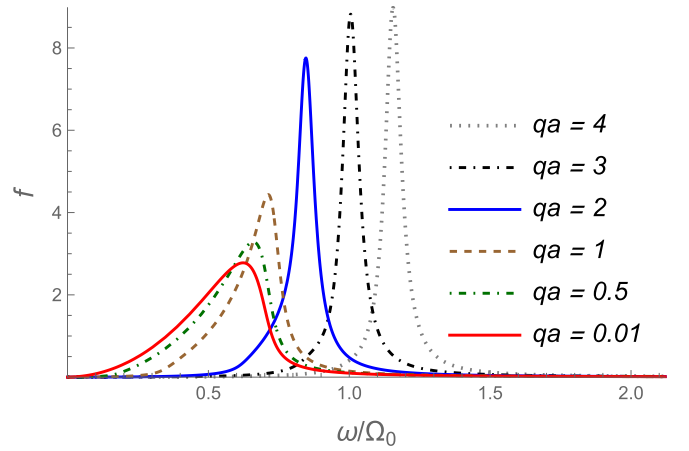

FIG. 9. Redistribution of spectral weight from the surface plasma frequency to the (bulk) plasmon continuum in the scaled surface loss function f in Eq. (27). The parameters used are $\epsilon = 2$, $\tau = 10/\Omega$, and the cutoff wave vector [determined through Eq. (5) by $\epsilon = 2$] $q^*a = \ln 3 \approx 1.1$. By construction, all curves have the same (unit) integrated weight. The frequency axis has been scaled by $\Omega_0 = \sqrt{\epsilon}\,\Omega$ to demonstrate the normalization; in these units, the plasmon continuum spans $0 < \omega < \Omega_0/\sqrt{\epsilon}$ in the long-wavelength limit.

density of a single layer, and the right-hand side of the f-sum rule in Eq. (23) can be evaluated as a geometric series to provide

$$\int_0^\infty d\omega\, \omega\, g(q,\omega) = \left(\frac{\pi \Omega_0^2}{8}\right) \frac{2|q|a}{1 - \exp(-2|q|a)}, \quad (24)$$

where

$$\Omega_0^2 := \frac{ne^2}{\epsilon_0 ma} = \epsilon\, \Omega^2 \quad (25)$$

is the unscreened optical plasma frequency.

The crucial consequence of the f-sum rule in Eq. (24) is that the $qa \to 0$ limit of the surface loss function remains finite:

$$\lim_{qa \to 0} \int_0^\infty d\omega\, \omega\, g(q,\omega) = \left(\frac{\pi \Omega_0^2}{8}\right). \quad (26)$$

The sharp $q \to 0$ surface plasmon in an isotropic metal exhausts the spectral weight required by the f-sum rule [21,28]; however, the semi-infinite Fetter model lacks this mode in the long-wavelength limit. Nevertheless, the f-sum rule is indifferent to whether sharp excitations are present: the contribution from the bulk plasmon continuum must compensate for the lost spectral weight at the surface plasmon peak. To demonstrate how this spectral weight is redistributed across the cutoff wave vector q^*, we can scale the surface loss function according to the f-sum rule in Eq. (24) as

$$f(q,\omega) := \left[\left(\frac{8}{\pi \Omega_0^2}\right) \frac{1 - \exp(-2|q|a)}{2|q|a}\right] \omega\, g(q,\omega), \quad (27)$$

so that f has unit weight $\int_0^\infty d\omega\, f(q,\omega) = 1$. One should note that the rescaling in Eq. (27) slightly distorts the spectrum of f (compared with the surface loss function g) due to the multiplicative factor of ω. In Fig. 9, the dispersion of f at $\epsilon = 2$ and $\tau = 10/\Omega$ is shown across several values of qa to demonstrate the rearrangement of spectral weight as the

surface plasmon peak is suppressed below $q^*a = \ln 3 \approx 1.1$ [using Eq. (5) for $\epsilon = 2$].

Before comparing our results with existing data, we should acknowledge that the model presented in Sec. II—the semi-infinite Fetter model (see Fig. 3)—contains several simplifying approximations. When describing the conducting planes, the planar conductivity $\sigma(\omega)$ in Eq. (1) was characterized by a constant relaxation time τ up to or in the $q > q^*$ regime beyond the plasma frequency, and we neglected dispersion with the planar wave vector q. The lack of dispersion means that we should restrict our analysis to the long-wavelength limit $ql \ll 1$, where l is the planar lattice spacing. If the interlayer distance between conducting planes a is sufficiently larger than the planar lattice spacing (i.e., $l \ll a$), then the surface loss function g of Eq. (15) can disperse with qa while maintaining $ql \ll 1$. Additionally, we chose to model the insulating layers by frequency-independent dielectric constants. If the bandgap of the dielectric layers is sufficiently large compared with the bulk or surface plasmon energies under consideration, we are primarily neglecting the low-energy phonon contributions of these insulating regions.

The approximations used in our simplified Fetter model of Sec. II are consistent with a long-wavelength analysis of the layered structure in the high-T_C cuprate superconductors. To be specific, we will consider the structure of Bi-2212 (also modeled within a system of conducting layers in Ref. [45]), which is characterized by the interbilayer distance between copper oxide planes $a \approx 15.4$ Å and the planar (nearest-neighbor Cu-Cu) lattice spacing $l \approx 3.8$ Å [50]. The small value $l/a \approx 0.25$ permits the surface loss function g of Eq. (15) to disperse with qa while remaining in the (planar) long-wavelength limit of $ql \ll 1$. While the low-frequency scattering rate $1/\tau(\omega)$ is famously linear in cuprates near optimal doping, the linearity of $1/\tau(\omega)$ in Bi-2212 begins to deviate near excitation energies of $\hbar\omega \sim 0.37$ eV [51]. The relaxation time $\tau(\omega)$ eventually saturates to a constant near $\hbar\omega \sim 0.62$ eV [51], which is well below the optical plasmon energy of doped Bi-2212 ($\hbar\Omega \sim 1$ eV from the optically determined loss function [12,52,53]). More subtly, Bi-2212 is a bilayer cuprate with two closely spaced copper oxide planes repeated every $a \approx 15.4$ Å (i.e., we neglect the planar lattice shift of the full $c \approx 30.8$ Å unit cell [50]). This bilayer structure in a layered electron gas results in an additional narrow band of acoustic modes [11,16,54] below the (bulk) plasmon continuum; however, the dispersion shown in Fig. 2 remains intact and qualitatively unaltered. As a result, we will neglect these lower-energy acoustic modes and focus on the broader plasmon continuum that occurs in the single-layer Fetter model of Fig. 3.

HREELS measurements of Bi-2212 at long wavelengths [12,55,56] corroborate the broad spectrum and (low energy) linear tail of our dielectric model, which can be seen in Figs. 6 and 7 at various relaxation times and dielectric constants, respectively. Due to the large interbilayer spacing of Bi-2212, the long-wavelength regime of the surface loss function is set by the small wave vector $1/a \approx 0.06$ Å^{-1}; using Eq. (5), we can approximate the cutoff wave vector as $q^* \approx 0.03$ Å^{-1} from the value $\epsilon \approx 4.5$ [12,51,53]. In this regime, HREELS studies [12,55,56] observe a broad peak, i.e., a peak with

full width at half maximum wider than the plasmon peak in Bi-2212 inferred via optical means [12,53,57,58], centered near the optical plasma frequency which, in our model, is associated with the broad spectrum of bulk plasmon excitation (i.e., the dispersion in Fig. 2 at small qa). Unfortunately, significant damping—either the result of the (insulating) cap layer [45] or some other cuprate behavior—at larger wave vectors (detailed in Refs. [55,56]) prevents tracking the dispersion of this broad spectrum beyond the long-wavelength limit; consequently, the regime of surface plasmon propagation for $q \gg q^*$ is not observed. This discrepancy suggests that the planar conductivity—or as discussed in Refs. [55,56], the polarizability—disperses in a nontrivial manner beyond the long-wavelength limit. As an additional complication, the low-energy incident electrons used in HREELS result in a skewed spectrum for long-wavelength scattering near the wave vector resolution [12,59,60]. The peak structure of broad, electronvolt-scale losses can be entirely washed out at these long wavelengths [12,56], rendering the surface loss function difficult to extract in Bi-2212. Nevertheless, correcting for this distorted spectrum appears to recover a long-wavelength surface loss function that scales linearly at low energies [12] rather than the quadratic tail observed in optical studies of the (bulk) loss function [52,53]. In our model, this linear tail is associated with the broad plasmon continuum at long wavelengths (see Fig. 2). Further, both a broad peak near the optical plasma frequency and (low energy) linear tail were observed in the HREELS spectrum of the related single-layer compound Bi-2201 [12], which suggests that these features are related to the cuprate layering structure.

VI. SUMMARY

EELS in a reflection geometry (HREELS) is often understood as a surface probe whose characteristic long-wavelength excitation is the surface plasmon. In the semi-infinite Fetter model (see Fig. 3), however, the extreme limit of conduction anisotropy restricts surface plasmon propagation to finite in-plane wave vectors q above a cutoff value q^*. Below q^*, the system lacks a surface plasmon and, therefore, has only the (bulk) plasmon as its collective, long-wavelength excitation. As the plane of reflection explicitly breaks translation symmetry, the plasmon contributes a continuum of excitations due to the nonconserved out-of-plane wave vector. To understand how this continuum might be observed in an HREELS experiment, we have employed a dielectric analysis to calculate the surface loss function—the material response probed by HREELS—of the semi-infinite Fetter model.

Our results can largely be summarized by Fig. 5. At sufficiently large $q > q^*$ in Figs. 5(a) and 5(b), the surface loss function g of Eq. (15) is characterized by a sharp surface plasmon peak with only a weak [or in Fig. 5(a), imperceptible] shoulder across the plasmon continuum. Just below q^* in Fig. 5(c), the surface plasmon peak becomes actively suppressed, and the plasmon continuum receives significant spectral weight. In Fig. 5(d), the long-wavelength limit has successfully suppressed the nonpropagating surface plasmon peak, and all that remains in the surface loss function is a broad response across the plasmon continuum [see Fig. 6(a) or 7(b)]. While the shape of the surface loss function requires

a calculation, our results can be understood within the context of the f-sum rule in Eq. (23) governing the semi-infinite Fetter model in Eq. (24). Whether there exist sharp excitations in the long-wavelength limit, the surface loss function must contain significant spectral weight in Eq. (26). Consequently, the long-wavelength surface loss function becomes a probe of the bulk plasmon continuum in the semi-infinite Fetter model.

[1] A. L. Fetter, Ann. Phys. **88**, 1 (1974).

[2] Y. Ando, K. Segawa, S. Komiya, and A. N. Lavrov, Phys. Rev. Lett. **88**, 137005 (2002).

[3] S. Komiya, Y. Ando, X. F. Sun, and A. N. Lavrov, Phys. Rev. B **65**, 214535 (2002).

[4] T. Watanabe, T. Fujii, and A. Matsuda, Phys. Rev. Lett. **79**, 2113 (1997).

[5] G. S. Boebinger, Y. Ando, A. Passner, T. Kimura, M. Okuya, J. Shimoyama, K. Kishio, K. Tamasaku, N. Ichikawa, and S. Uchida, Phys. Rev. Lett. **77**, 5417 (1996).

[6] M. Hepting, L. Chaix, E. W. Huang, R. Fumagalli, Y. Y. Peng, B. Moritz, K. Kummer, N. B. Brookes, W. C. Lee, M. Hashimoto *et al.*, Nature (London) **563**, 374 (2018).

[7] J. Lin, J. Yuan, K. Jin, Z. Yin, G. Li, K.-J. Zhou, X. Lu, M. Dantz, T. Schmitt, H. Ding *et al.*, npj Quantum Mater. **5**, 4 (2020).

[8] A. Nag, M. Zhu, M. Bejas, J. Li, H. C. Robarts, H. Yamase, A. N. Petsch, D. Song, H. Eisaki, A. C. Walters *et al.*, Phys. Rev. Lett. **125**, 257002 (2020).

[9] A. Singh, H. Y. Huang, C. Lane, J. H. Li, J. Okamoto, S. Komiya, R. S. Markiewicz, A. Bansil, A. Fujimori, C. T. Chen *et al.*, Phys. Rev. B **105**, 235105 (2022).

[10] See Supplemental Material at http://link.aps.org/supplemental/10.1103/PhysRevLett.125.257002.

[11] K. Schulte, D. Dulić, and G. Sawatzky, Physica C **317-318**, 554 (1999).

[12] K. H. G. Schulte, The Interplay of Spectroscopy and Correlated Materials, Ph.D. thesis, University of Groningen, 2002.

[13] F. Gabriele, C. Castellani, and L. Benfatto, Phys. Rev. Res. **4**, 023112 (2022).

[14] D. Grecu, Phys. Rev. B **8**, 1958 (1973).

[15] N. C. Constantinou and M. G. Cottam, J. Phys. C **19**, 739 (1986).

[16] E. L. Albuquerque and M. G. Cottam, in *Polaritons in Periodic and Quasiperiodic Structures*, edited by E. L. Albuquerque and M. G. Cottam (Elsevier Science, Amsterdam, 2004), pp. 65–87.

[17] J. K. Jain and P. B. Allen, Phys. Rev. B **32**, 997 (1985).

[18] M. Apostol, Z. Phys. B **22**, 13 (1975).

[19] G. F. Giuliani and J. J. Quinn, Phys. Rev. Lett. **51**, 919 (1983).

[20] G. D. Mahan, J. Phys.: Condens. Matter **24**, 305003 (2012).

[21] B. Gumhalter and D. Newns, Phys. Lett. A **53**, 137 (1975).

[22] A. Griffin and J. Harris, Can. J. Phys. **54**, 1396 (1976).

[23] A. G. Eguiluz, Phys. Rev. B **23**, 1542 (1981).

[24] B. Gumhalter, Prog. Surf. Sci. **15**, 1 (1984).

[25] A. Liebsch, *Electronic Excitations at Metal Surfaces*, 1st Ed., Physics of Solids and Liquids (Springer Science+Business Media, LLC, New York, 1997).

[26] A. A. Husain, E. W. Huang, M. Mitrano, M. S. Rak, S. I. Rubeck, X. Guo, H. Yang, C. Sow, Y. Maeno, B. Uchoa *et al.*, arXiv:2007.06670 (2020).

[27] A. Bergara, J. Pitarke, and R. Ritchie, Phys. Lett. A **256**, 405 (1999).

[28] A. García-Lekue and J. M. Pitarke, Phys. Rev. B **64**, 035423 (2001).

[29] R. Ritchie, On the Interaction of Charged Particles with Plasma, Ph.D. thesis, University of Tennessee, 1959.

[30] D. Mills, Surf. Sci. **48**, 59 (1975).

[31] S. Vig, A. Kogar, M. Mitrano, A. A. Husain, V. Mishra, M. S. Rak, L. Venema, P. D. Johnson, G. D. Gu, E. Fradkin *et al.*, SciPost Phys. **3**, 026 (2017).

[32] E. Evans and D. L. Mills, Phys. Rev. B **5**, 4126 (1972).

[33] R. E. Camley and D. L. Mills, Phys. Rev. B **29**, 1695 (1984).

[34] A. Lucas and M. Šunjić, Prog. Surf. Sci. **2**, 75 (1972).

[35] R. H. Ritchie, Phys. Rev. **106**, 874 (1957).

[36] M. G. Cottam and D. R. Tilley, *Introduction to Surface and Superlattice Excitations* (Cambridge University Press, Cambridge, 1989).

[37] B. N. J. Persson and E. Zaremba, Phys. Rev. B **31**, 1863 (1985).

[38] V. U. Nazarov, Phys. Rev. B **49**, 17342 (1994).

[39] A. A. Lucas and M. Šunjić, Phys. Rev. Lett. **26**, 229 (1971).

[40] A. Lucas, J. Vigneron, P. Lambin, P. Thiry, M. Liehr, J. Pireaux, and R. Caudano, Int. J. Quantum Chem. **28**, 687 (1985).

[41] J. K. Jain, Phys. Rev. B **32**, 5456 (1985).

[42] J. K. Jain and P. B. Allen, Phys. Rev. Lett. **54**, 947 (1985).

[43] R. Egerton, *Electron Energy-Loss Spectroscopy in the Electron Microscope*, 3rd Ed. (Springer US, New York, 2011).

[44] E. Albuquerque and M. Cottam, Phys. Rep. **233**, 67 (1993).

[45] D. L. Mills, R. B. Phelps, and L. L. Kesmodel, Phys. Rev. B **50**, 6394 (1994).

[46] P. Lambin, J. Vigneron, and A. Lucas, Solid State Commun. **54**, 257 (1985).

[47] P. Lambin, J. P. Vigneron, and A. A. Lucas, Phys. Rev. B **32**, 8203 (1985).

[48] P. Lambin, J. P. Vigneron, A. A. Lucas, and A. Dereux, Phys. Scr. **35**, 343 (1987).

[49] B. Gumhalter, Calculation of Dynamic Screening Effects in the Optical Properties of Chemisorbed Species, Ph.D. thesis, Imperial College London, 1976.

[50] P. Villars, Bi-2212 ($Sr_2CaCu_2Bi_2O_8$) crystal structure, in *Inorganic Solid Phases, SpringerMaterials (online database)* (Springer-Verlag GmbH, Heidelberg, 2016).

[51] D. v. d. Marel, H. J. A. Molegraaf, J. Zaanen, Z. Nussinov, F. Carbone, A. Damascelli, H. Eisaki, M. Greven, P. H. Kes, and M. Li, Nature (London) **425**, 271 (2003).

[52] I. Bozovic, Phys. Rev. B **42**, 1969 (1990).

[53] J. Levallois, M. K. Tran, D. Pouliot, C. N. Presura, L. H. Greene, J. N. Eckstein, J. Uccelli, E. Giannini, G. D. Gu, A. J. Leggett *et al.*, Phys. Rev. X **6**, 031027 (2016).

[54] G. Qin, G. F. Giuliani, and J. J. Quinn, Phys. Rev. B **28**, 6144 (1983).

[55] M. Mitrano, A. A. Husain, S. Vig, A. Kogar, M. S. Rak, S. I. Rubeck, J. Schmalian, B. Uchoa, J. Schneeloch, R. Zhong *et al.*, Proc. Natl. Acad. Sci. USA **115**, 5392 (2018).

[56] A. A. Husain, Charge Fluctuations of the Strange Metal in Space and Time, Ph.D. thesis, University of Illinois at Urbana-Champaign, 2020.

[57] C. Presura, Energetics and Ordering in Strongly Correlated Oxides as seen in Optics, Ph.D. thesis, University of Groningen, 2003.

[58] I. Bozović, J. H. Kim, J. S. Harris, and W. Y. Lee, Phys. Rev. B **43**, 1169 (1991).

[59] R. E. Palmer, J. F. Annett, and R. F. Willis, Phys. Rev. Lett. **58**, 2490 (1987).

[60] J. Li, Z. Lin, G. Miao, W. Zhong, S. Xue, Y. Li, Z. Tao, W. Wang, J. Guo, and X. Zhu, Surf. Sci. **721**, 122067 (2022).